

Dynamical variational Monte Carlo as a quantum impurity solver: Application to cluster dynamical mean field theory

P. Rosenberg ¹, D. Sénéchal ¹, A.-M. S. Tremblay ¹ and M. Charlebois ^{1,2}

¹*Département de Physique, RQMP & Institut Quantique, Université de Sherbrooke, Sherbrooke, Québec J1K 2R1, Canada*

²*Département de Chimie, Biochimie et Physique, Institut de Recherche sur l'Hydrogène, Université du Québec à Trois-Rivières, Trois-Rivières, Québec G9A 5H7, Canada*



(Received 28 July 2023; accepted 6 November 2023; published 8 December 2023)

Two of the primary sources of error in the Cluster dynamical mean field theory (CDMFT) technique arise from the use of finite size clusters and finite size baths, which makes the development of impurity solvers that can treat larger systems an essential goal. In this work we introduce an impurity solver based on the recently developed dynamical variational Monte Carlo (dVMC) method. Variational Monte Carlo possesses a favorable scaling as a function of system size, which enables the treatment of systems beyond the reach of current exact diagonalization solvers. To benchmark the technique, we perform a systematic set of CDMFT calculations on the single-band one-dimensional Hubbard model. We compare to results obtained with an exact diagonalization solver for small clusters, and against the exact solution in the thermodynamic limit obtained by Lieb and Wu for larger clusters. The development of improved impurity solvers will help extend the reach of quantum cluster methods, which can be applied to a wide range of strongly correlated electron systems, promising new insights into their emergent behavior.

DOI: [10.1103/PhysRevB.108.245122](https://doi.org/10.1103/PhysRevB.108.245122)

I. INTRODUCTION

Strongly correlated many-electron systems are one of the central challenges of condensed matter physics. These systems generally do not permit exact solutions, except for selected limiting cases. The lack of robust quantitative descriptions of these systems necessitates the development of ever-improving approximative and numerical approaches [1]. One set of computational techniques that have proved quite successful in the treatment of strongly correlated electrons is the quantum cluster methods, comprising cluster perturbation theory (CPT) [2–4], cluster dynamical mean-field theory (CDMFT), and dynamical cluster approximation (DCA) [5–11], among others.

The principle underlying these techniques is to represent the system as a finite size cluster embedded in an infinite lattice. The self-energy of the cluster can then be used to approximate the self-energy of the infinite system. The effect of the infinite lattice on the cluster is incorporated by adding additional terms to the cluster Hamiltonian, or, in the case of CDMFT, bath degrees of freedom whose values are determined self-consistently.

One of the central components of the CDMFT procedure is to solve the cluster-bath problem using a so-called impurity solver [12,13]. For discrete bath representations, most current impurity solvers are based on exact diagonalization, which is limited to fairly small cluster sizes given the exponential scaling of the algorithm with the dimension of the Hilbert space. This limitation leads to the two sources of systematic error in the CDMFT technique: finite size clusters and finite size baths [14]. In the limit of infinite cluster size, the CDMFT result represents the thermodynamic limit; however, for small

clusters the finite size error can be significant. Unlike the case of an infinite cluster, an infinite bath connected to a finite cluster does not represent the thermodynamic limit, but larger baths provide an improved representation of the effect of the environment on the cluster. The development of impurity solvers that can treat larger clusters will help minimize these fundamental sources of error and improve the capability of this already powerful method.

In this work we introduce an impurity solver for CDMFT based on the dynamical variational Monte Carlo technique (dVMC) [15]. This approach is sign-problem free and scales polynomially with system size, which permits the treatment of cluster sizes beyond the reach of current exact diagonalization solvers. These benefits, however, come at the cost of statistical errors inherent to all Monte Carlo approaches and systematic errors due to the *Ansatz* for the ground state and excitations. The method has already demonstrated impressive accuracy as an impurity solver in CPT calculations on the hole-doped two-dimensional Hubbard model [16], and here we extend and apply the technique within CDMFT. To gauge the accuracy of the approach we perform a set of benchmarks on the single-band one-dimensional (1D) Hubbard model. We compare our CDMFT-dVMC results to CDMFT-ED results on small to intermediate size clusters before treating larger clusters, whose results are compared to the exact solution obtained by Lieb and Wu [17].

While we benchmark against the Lieb-Wu solution, which provides only ground state properties, we emphasize that this technique is designed to compute dynamical properties, such as the spectral function, as we demonstrate below. Related techniques based on variational Monte Carlo have been developed to access dynamical quantities [18], but these approaches

focused on the charge or spin structure factors [19–22], or the neutron resonance mode [23], as opposed to the Green function, which is an essential ingredient in quantum cluster methods.

We organize the remainder of the paper as follows. We introduce the method in Sec. II. In Sec. III we present a set of benchmarks, first for small and intermediate clusters, followed by large clusters. Finally, we discuss the performance of the method and possible improvements in Sec. IV. Details of the technique are provided in a set of appendices.

II. METHOD

The method we present in this work is based on the dVMC technique introduced in Ref. [15], which was designed to treat systems with periodic boundary conditions and translational invariance. The technique was recently extended to treat systems with open boundary conditions, which enables its use as an impurity solver in various quantum cluster methods [16]. In Ref. [16] the technique was applied within CPT, which does not include bath sites, nor does it involve a self-consistency procedure. Here we implement the approach within CDMFT, which includes both of these ingredients.

In this section, we present some relevant details of the generalized dVMC method; a more complete discussion can be found in Refs. [15,16]. In the Supplemental Material [24], the reader can find the code implementing the algorithm described here, which was used to obtain the results presented below.

A. Green function from generalized dVMC

As in Refs. [15,16], the generalized dVMC technique uses variational Monte Carlo to optimize a ground state *Ansatz* describing a system of N_e electrons, which is then used to obtain the Green function. Within the generalized dVMC approach, the Green function matrix at a complex frequency z is computed according to [16]

$$\mathbf{G}^\pm(z) = \mathbf{S}((z \pm \Omega)\mathbb{1} \mp \mathbf{H})^{-1} \mathbf{S} \quad (1)$$

$$= \mathbf{Q}((z \pm \Omega)\mathbb{1} \mp \mathbf{E})^{-1} \mathbf{Q}^\dagger, \quad (2)$$

where \mathbf{S} is the overlap matrix of the non-orthogonal basis used to express the one particle excited sectors of the Hamiltonian operator in matrix form: \mathbf{H} . $\mathbf{Q} \equiv \mathbf{S}^{1/2} \mathbf{U}$ and \mathbf{U} and \mathbf{E} are the eigenvectors and eigenvalues respectively of the matrix $\mathbf{M} \equiv \mathbf{S}^{-1/2} \mathbf{H} \mathbf{S}^{-1/2}$. To understand this formula intuitively, recall that the Green function is obtained from states with one more or one less particle compared with the ground state. These states are obtained [15,16] from an algorithm that generates independent but nonorthogonal basis states whose overlap is represented by the matrix \mathbf{S} .

The matrices \mathbf{S} and \mathbf{H} are of dimension $2NN_{\text{exc}}$, where N is the number of sites and N_{exc} is the number of single-particle excitations, i.e., the number of many-body states containing one more (fewer) electron than the ground state. We select a physically motivated subset of all possible single-particle excitations based on locality [15,16].

The factor of 2 reflects the presence of two spin species; in the case of one spin species, these matrices are of dimension NN_{exc} . The matrix elements of \mathbf{S} and \mathbf{H} are computed with

respect to the variational ground state, obtained according to the algorithm described in Refs. [15,16,25,26]. The plus and minus signs of Eq. (1) refer to the electron and hole Green function matrices respectively, and they have been omitted from the matrices \mathbf{S}^\pm , \mathbf{H}^\pm , etc. to remain concise.

As in Ref. [16], we apply a filtering algorithm to the overlap matrix \mathbf{S} to reduce Monte Carlo noise and ensure that the matrix is positive definite. In Ref. [16], the filtering procedure removed only negative eigenvalues of the overlap matrix. Here we perform an additional filtering, which removes the very small positive eigenvalues of the overlap matrix. In order to determine the number of states to filter, we perform a singular value decomposition, $\mathbf{S} = \mathbf{U}_{\text{SVD}} \mathbf{\Sigma}_{\text{SVD}} \mathbf{V}_{\text{SVD}}^\dagger$, where the matrix $\mathbf{\Sigma}_{\text{SVD}} = \text{diag}(s_1, s_2, \dots, s_{NN_{\text{exc}}})$ contains the singular values of \mathbf{S} . Note that $\mathbf{\Sigma}_{\text{SVD}}$ is *not* related to the self-energy $\mathbf{\Sigma}(\omega)$ defined below. The smallest singular value we keep is given by $s_{\text{min}} = (s_{\text{max}}) \times 10^{-k}$, where k is a condition number. We fix this condition number, for the sake of consistency, to $k = 6$. Everything below s_{min} is filtered as detailed in Ref. [16].

The Green function is then obtained by summing the electron and hole Green function matrices and keeping only the sector corresponding to the trivial excitation, $m = n = 0$, namely $c^{(\dagger)}|\Omega\rangle$:

$$G_{ij,\sigma}(z) = [\mathbf{G}^+(z) + \mathbf{G}^-(z)]_{ij,\sigma=\sigma',m=n=0}, \quad (3)$$

where the indices i, j denote site numbers and m, n denote excitation numbers. Let us underline here that the boldface font used up until this point included i, j and m, n , but from now on it will include only i, j . Indeed, the m, n degrees of freedom are only necessary to sample the excited sectors of the Hamiltonian (\mathbf{H}^\pm), but not to express the cluster Green function $G_{ij,\sigma}(z)$.

B. Cluster dynamical mean field theory (CDMFT)

We implement the dVMC impurity solver within the CDMFT technique, so in this section we present the essential components of the CDMFT approach. In CDMFT, the infinite lattice system is modeled by an impurity Hamiltonian composed of a set of interacting cluster sites coupled to noninteracting bath sites. The impurity Hamiltonian has the general form

$$\begin{aligned} \hat{H}_{\text{imp}} = & \sum_{i,j,\sigma} (t_{ij} \hat{c}_{i\sigma}^\dagger \hat{c}_{j\sigma} + \text{H.c.}) + U \sum_i \hat{n}_{i\uparrow} \hat{n}_{i\downarrow} - \mu \sum_{i,\sigma} \hat{n}_{i\sigma} \\ & + \sum_{i\lambda,\sigma} (\theta_{i\lambda} \hat{c}_{i\sigma}^\dagger \hat{b}_{\lambda\sigma} + \text{H.c.}) + \sum_{\lambda} \varepsilon_{\lambda} \hat{b}_{\lambda\sigma}^\dagger \hat{b}_{\lambda\sigma}, \end{aligned} \quad (4)$$

where $\hat{c}_{i\sigma}$ annihilates an electron of spin $\sigma = \uparrow, \downarrow$ on a cluster site $i = 1, \dots, N_c$, and $\hat{b}_{\lambda\sigma}$ annihilates an electron of spin σ on a bath site labeled by $\lambda = 1, \dots, N_b$, where N_c and N_b are the numbers of cluster sites and bath sites, respectively. The bath is parametrized by cluster-bath hybridization terms, $\theta_{i\lambda}$, and bath site energies, ε_{λ} [14,27,28]. An illustration of the bath configuration used in this work is given in Fig. 1.

The cluster Green function, $\mathbf{G}_c(\omega)$, is obtained by the impurity solver, which provides an efficient means of extracting the self-energy $\mathbf{\Sigma}(\omega)$ at any complex frequency, ω . The Green function of the original lattice Hamiltonian can then be

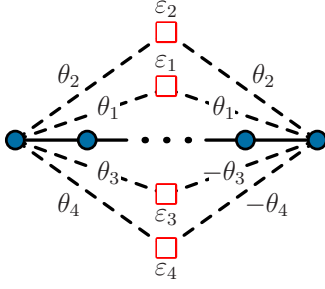


FIG. 1. Bath configuration. Bath sites couple to both edges of the cluster, with half of the bath sites belonging to the symmetric representation of the reflection symmetry, and the other half belonging to the antisymmetric representation. Symmetry considerations are useful to define bath parameters [28,34,35]. When more bath sites are used, the number of symmetric and antisymmetric independent baths remains the same.

computed using the cluster self-energy and the noninteracting lattice Green function, $\mathbf{G}_0(\tilde{\mathbf{k}}, \omega)$:

$$\mathbf{G}^{-1}(\tilde{\mathbf{k}}, \omega) = \mathbf{G}_0^{-1}(\tilde{\mathbf{k}}, \omega) - \Sigma(\omega). \quad (5)$$

The momentum $\tilde{\mathbf{k}}$ runs over the reduced Brillouin zone of the superlattice of clusters.

In order to compare the Green function of the lattice to that of the cluster, the lattice Green function is projected back onto the cluster,

$$\tilde{\mathbf{G}}(\omega) = \frac{N_c}{N} \sum_{\tilde{\mathbf{k}}} [\mathbf{G}_0^{-1}(\tilde{\mathbf{k}}, \omega) - \Sigma(\omega)]^{-1}. \quad (6)$$

The remainder of the CDMFT procedure consists in finding a set of bath parameters that makes the cluster Green function, $\mathbf{G}_c(\omega)$, and the projected lattice Green function, $\tilde{\mathbf{G}}(\omega)$, as close as possible to each other [11]. This can be done by minimizing a distance function [14,27]. A new cluster Green function can then be computed with this new set of bath parameters and the procedure is repeated until convergence. In the case of the dVMC impurity solver, we determine convergence by inspection of the bath parameters (see Appendix A). We note that the computational cost scales with the number of sites, $N_s = N_c + N_b$, as $N_s^{3.5}$, and the number of excitations as $N_{\text{exc}}^{1.5}$ [16], but with a larger prefactor in the case of CDMFT.

After convergence, the lattice Green function $\mathbf{G}(\tilde{\mathbf{k}}, \omega)$ [Eq. (5)] can then be used to compute the average value of observables. The average lattice density is computed with

$$n = \int_{-\infty}^0 d\omega \sum_{\tilde{\mathbf{k}}} \text{Tr}[\mathbf{G}(\tilde{\mathbf{k}}, \omega)]. \quad (7)$$

This will be the main focus of Sec. III.

III. RESULTS

A. Model

As an initial test of the CDMFT-dVMC technique, we perform a set of calculations on the single-band one-dimensional Hubbard model. This model has been solved exactly [17], and has been well studied by other numerical techniques [28–33],

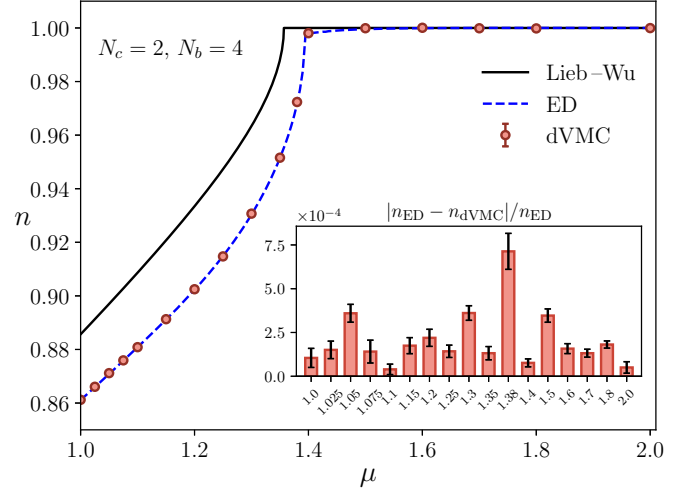


FIG. 2. Density versus chemical potential for a two site cluster with four bath sites. The inset shows the relative error between the result from the dVMC solver and the result from the ED solver at each value of μ studied. The error bars represent the error of the CDMFT-dVMC result (see Appendix A for details). Note that the same error is given in the inset as a fraction of the ED result. The exact result from Lieb and Wu [17] is given by the black curve.

which makes it an ideal testbed to assess the accuracy of the approach.

The model has the following Hamiltonian:

$$\hat{H} = \sum_{(ij),\sigma} -t(\hat{c}_{i\sigma}^\dagger \hat{c}_{j\sigma} + \text{H.c.}) + U \sum_i \hat{n}_{i\uparrow} \hat{n}_{i\downarrow} - \mu \sum_{i,\sigma} \hat{n}_{i\sigma}, \quad (8)$$

where t is the amplitude for nearest neighbor hopping, U is the on-site interaction strength, and μ is the chemical potential. In the results that follow we take $U/t = 4$.

B. Benchmark against ED solver

In this section we present a series of benchmark CDMFT calculations on small clusters, which provide a direct comparison of the performance of the dVMC impurity solver to that of an exact diagonalization solver.

We first study a cluster of two sites with four bath sites. We chose a bath configuration in which each bath site is connected to the edge sites at either end of the cluster, where two bath sites, with energies ε_1 and ε_2 , belong to the symmetric representation of the reflection symmetry and the other bath sites, with energies ε_3 and ε_4 , belong to the antisymmetric representation. The role of the bath sites is to represent the environment surrounding the cluster, therefore they couple only to the edges of the cluster. The bath configuration is illustrated in Fig. 1. These small clusters can be treated by exact diagonalization, which provides a reliable assessment of the accuracy of the dVMC solver.

In Fig. 2 we show the average lattice density computed via CDMFT versus chemical potential. We observe that the results obtained by the dVMC impurity solver (red circles) are in excellent agreement with the exact diagonalization results (ED, dashed blue line). As shown in the inset, the relative error is below 0.1% for the range of chemical potentials we have

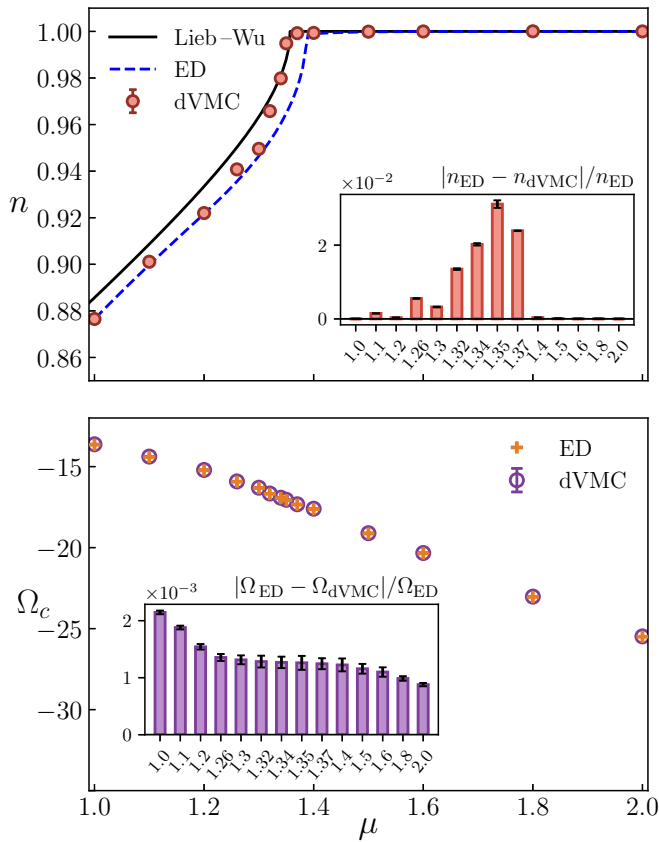


FIG. 3. Top: Average density versus chemical potential computed with dVMC and ED impurity solvers. The exact result from Lieb and Wu [17] is given by the black curve. Bottom: Grand potential (units of t) of the cluster versus chemical potential. The purple circles show the CDMFT-dVMC result and the orange crosses show the ED result computed with the bath parameters from the converged CDMFT-dVMC iterations. The error bars represent the error of the CDMFT-dVMC result (see Appendix A for details). Note that the same error is given in the inset as a fraction of the ED result. The system has $N_c = 8$ cluster sites, $N_b = 4$ bath sites, and $N_e = 12$ electrons.

considered, which spans from the metallic to the insulating state. This is an important initial demonstration of the capability of dVMC as a CDMFT impurity solver, indicating that it can reproduce the results of CDMFT with an ED impurity solver on small clusters with quantitative accuracy. Note that we also show the exact result obtained by Lieb and Wu for an infinite 1D interacting lattice from the Bethe Ansatz [17] as a black line throughout this paper. It is only a reference for now because in the best-case scenario we do not expect dVMC to obtain a result closer to the Lieb-Wu result than that obtained with ED.

Having calibrated the accuracy of the dVMC solver on small clusters, we proceed with a set of calculations on intermediate sized clusters. In the top panel of Fig. 3 we again show the average lattice density versus chemical potential, computed with the dVMC and exact diagonalization impurity solvers. We find that the dVMC results are in good agreement with the exact diagonalization results in both the metallic and insulating limits, for values of $\mu < 1.3$ and $\mu > 1.4$. In the

region near the transition between the metallic and insulating states, $\mu \in [1.32, 1.38]$, the dVMC results are in qualitative agreement with the exact diagonalization results; however, the dVMC impurity solver obtains a different value of the critical chemical potential μ_c , which indicates the edge of the gap. The dVMC curve still shows a sharp increase in slope as the chemical potential approaches μ_c , but this increase occurs at a slightly lower value of chemical potential than the corresponding exact diagonalization result.

In order to better understand the behavior of the dVMC solver, we next consider the accuracy of the ground state of the cluster obtained by the solver. The bottom panel of Fig. 3 shows the grand potential of the cluster, Ω_c , versus chemical potential. In the top panel, at each chemical potential, the dVMC value represents the average over the converged CDMFT iterations (see Appendix A), whereas the ED result is the value at the final CDMFT iteration. In the bottom panel, the dVMC value is again obtained by averaging over the converged iterations, whereas the ED value is computed using the bath parameters from the converged CDMFT-dVMC iterations. The grand potential of the cluster computed by dVMC is generally in excellent agreement with the exact diagonalization result, typically within $\sim 0.2\%$. The dVMC result tends to become more accurate as a function of increasing chemical potential, with the most accurate results being obtained after the transition to the insulating state above $\mu \sim 1.4$. We note, however, that the error bars are largest in the region near μ_c [28], for $\mu \in [1.3, 1.6]$. This suggests that the ground state energy landscape in this region is complicated, which is reflected in the larger variance in the representation of the ground state achieved by the dVMC solver. The ground state energy of a dVMC solution has many potential sources of noise; note that the fluctuations between VMC iterations are of the same order or smaller than those between CDMFT iterations. See Appendix C for a detailed analysis. The dVMC description of the ground state is a subject we will touch upon in a later section.

As highlighted above, the ability to compute dynamical properties of strongly correlated systems is one of the central motivations behind the development of this technique. We therefore proceed by computing the spectral function, $A(k, \omega)$, for several of the systems presented in Fig. 3. To further gauge the accuracy of the dVMC impurity solver we compute the same quantity with both the dVMC and exact diagonalization solvers. In the top row of Fig. 4 we present the spectral function versus average density obtained with the exact diagonalization impurity solver and in the bottom row we show the result obtained with the dVMC solver.

We find that the CDMFT-dVMC results capture the same basic qualitative features as the CDMFT-ED results. In both sets of calculations, a single band crosses the Fermi level at lower density, which gradually loses spectral weight until a gap opens that is symmetric about the Fermi level at half filling.

Finally, to complement the results presented above, we compute the local density at several values of chemical potential. As in earlier results, the CDMFT-dVMC values are obtained by averaging over the set of converged iterations, whereas the CDMFT-ED values are taken from the final CDMFT-ED iteration.

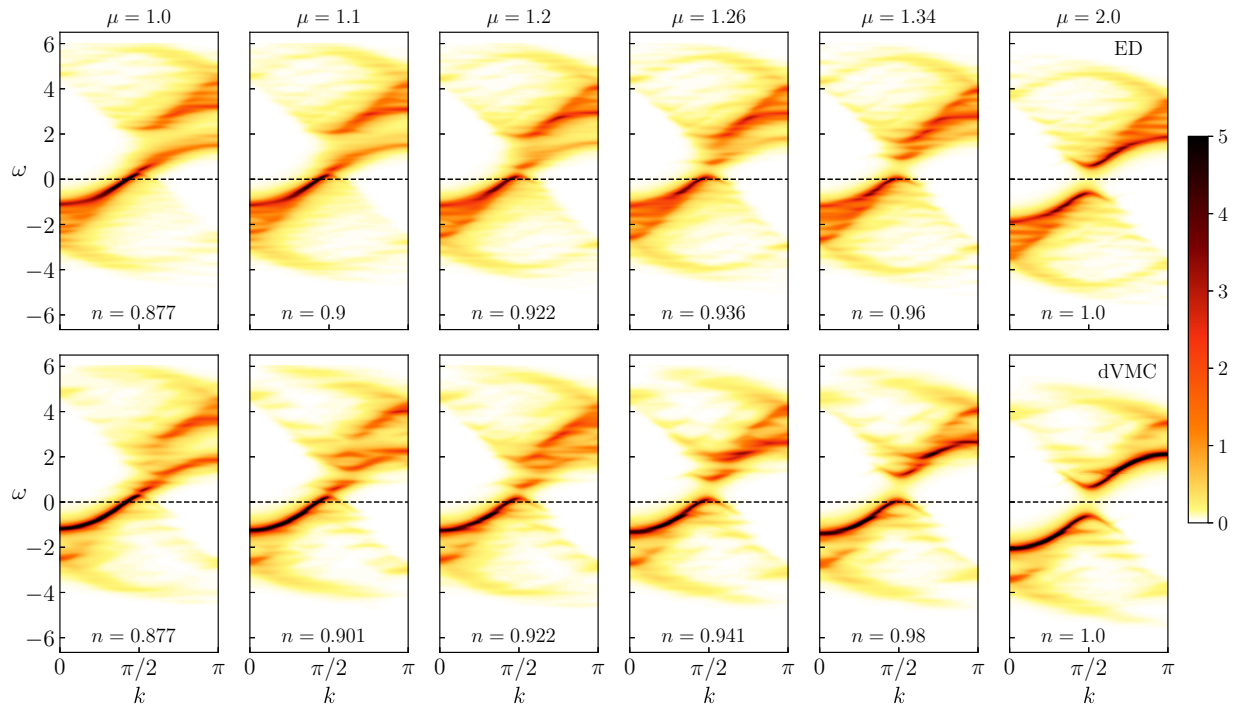


FIG. 4. $A(k, \omega)$ versus average density for $N_c = 8$ and $N_b = 4$ system from CDMFT-ED (top row) and CDMFT-dVMC (bottom row). Each column corresponds to a specific μ , with the resulting average lattice density given at the bottom of each plot.

The CDMFT-dVMC results for the local density are generally in good quantitative agreement with the CDMFT-ED results (Fig. 5). At smaller values of chemical potential (top row) the CDMFT-ED result shows an oscillatory feature that the CDMFT-dVMC results match to within $\sim 1\%$ error. At larger values of chemical potential (bottom row) the

CDMFT-dVMC results are even more accurate, in this case within $\sim 0.25\%$ of the CDMFT-ED result.

C. Results for large systems

In the preceding sections we presented a thorough set of benchmarks on small and intermediate sized clusters to establish the accuracy of the dVMC impurity solver within CDMFT. Here we perform a set of calculations on large clusters, beyond the reach of exact diagonalization solvers. The ability to treat larger clusters reduces finite size effects and provides a clearer understanding of the behavior of the method as a function of the number of cluster sites as well as bath sites. Our results for the average lattice density versus chemical potential are summarized in Fig. 6.

We used two different clusters for this set of calculations, both with 24 total sites. We observe that for small to intermediate chemical potential ($\mu \leq 1.2$) the 20 site cluster with 4 bath sites ($20 + 4$) and the 16 site cluster with 8 bath sites ($16 + 8$) both obtain results for the average density in good agreement with the Lieb-Wu result, generally within $\sim 1\%$. Similarly to the results for smaller clusters, the agreement between the CDMFT-dVMC result and the Lieb-Wu result is somewhat worse towards the transition to the insulating state. The Monte Carlo estimate of the error is also larger in this region, suggesting a potentially complicated ground state landscape that poses a challenge for the dVMC approach, which is consistent with the previous benchmark against ED shown in Fig. 3. For chemical potentials beyond the transition, the CDMFT-dVMC results are exceptionally accurate.

In Fig. 7 we show the spectral function versus average density for the $16 + 8$ system (top row) and the $20 + 4$ system (bottom row). The results for both clusters reliably capture the

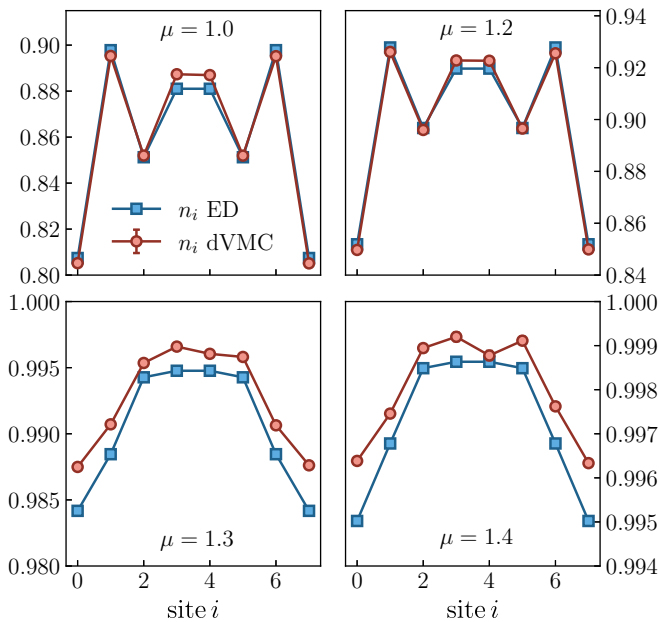


FIG. 5. Local density, n_i , versus cluster site, i , from CDMFT-dVMC and CDMFT-ED. Each system has $N_c = 8$ cluster sites, $N_b = 4$ bath sites, and $N_e = 12$ electrons.

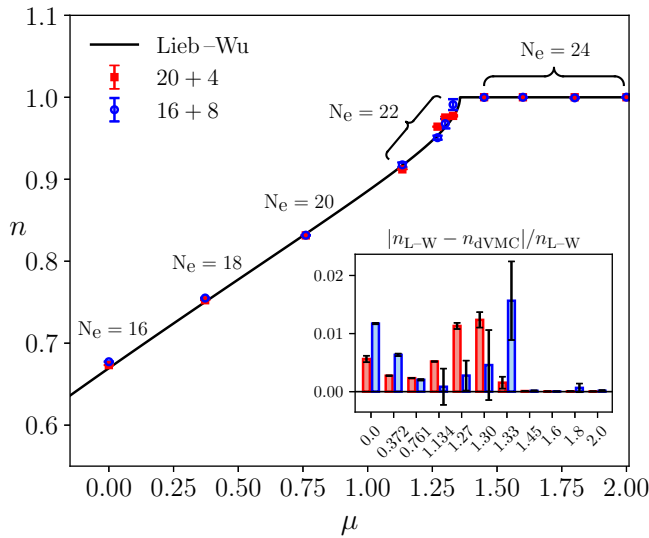


FIG. 6. Average density versus chemical potential for systems with 24 total sites. The exact Lieb-Wu result is given by the black curve. Inset: Relative error between Lieb-Wu result and CDMFT result with dVMC impurity solver at each value of μ (given by the x axis) studied. The error bars represent the error of the CDMFT-dVMC result (see Appendix A for details). Note that the same error is given in the inset as a fraction of the ED result. The number of electrons, N_e , for each calculation is given above the corresponding data point or set of data points.

major qualitative features of the physics at increasing values of average density [33]. At low density there is a single band with significant spectral weight crossing the Fermi level. As the density increases, this band loses spectral weight above the Fermi level and eventually a gap opens, with the Fermi level lying in the middle of the gap at the particle-hole symmetric point ($\mu = 2.0$ in this case). The differences between the results presented in the top row of Fig. 7 and the bottom row provide a good estimate of the error or imprecision of the method. While the average densities are not identical for the two systems, they capture the same physics and qualitative behavior of the spectral function. Importantly, despite the small discrepancies between these two sets of results, the quality of the spectra is considerably improved, and less discretized, than the result for smaller clusters, from ED or dVMC (Fig. 4), which shows visible finite size effects.

Finally, we compute the local density at several values of average total lattice density for both clusters. Far from half filling (upper left panels of Figs. 8 and 9), the local density shows a modulation that is likely induced by the finite size of the lattice in combination with the particular value of total average lattice density. No charge order is observed in the Lieb-Wu solution. As the total density increases, this oscillation disappears and the local density becomes more uniform towards the center of the cluster. At half filling the local density is essentially constant, as expected.

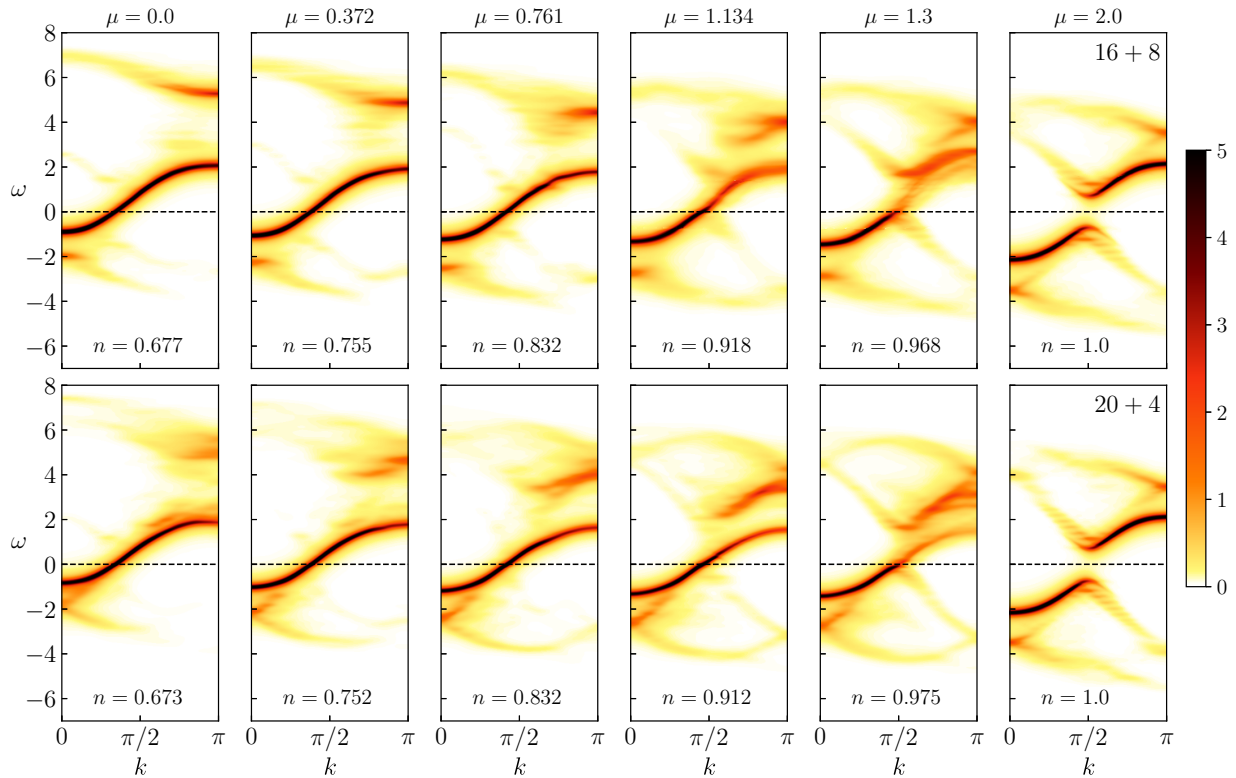


FIG. 7. $A(k, \omega)$ versus average density for $N_c = 16$ and $N_b = 8$ (top row) and $N_c = 20$ and $N_b = 4$ (bottom row) systems from CDMFT-dVMC. Each column corresponds to a specific μ , with the resulting average lattice density given at the bottom of each plot.

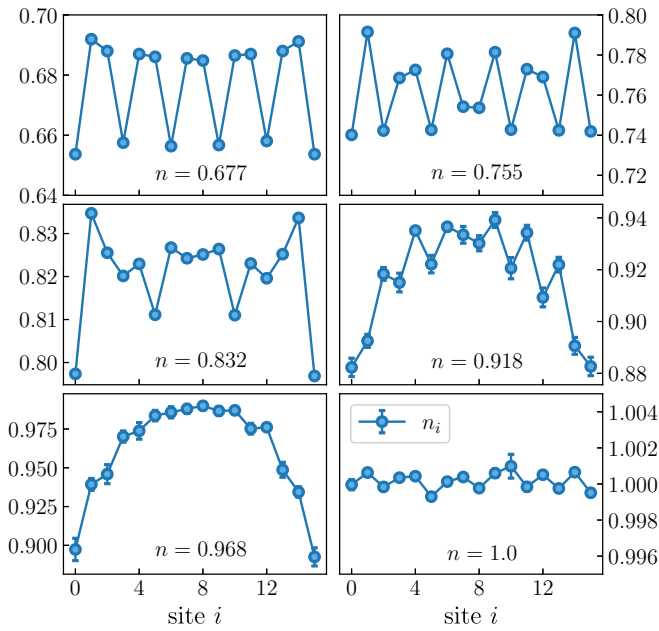


FIG. 8. Local density, n_i , versus cluster site, i , at various values of total average density for a $16 + 8$ system. An oscillation in the local density, likely related to the finite cluster size and average density, is evident at $n = 0.677$. This oscillation disappears at larger values of average density until the local density is essentially constant at $n = 1.0$.

IV. DISCUSSION

In this section we note some of the remaining technical challenges that currently limit the performance of the

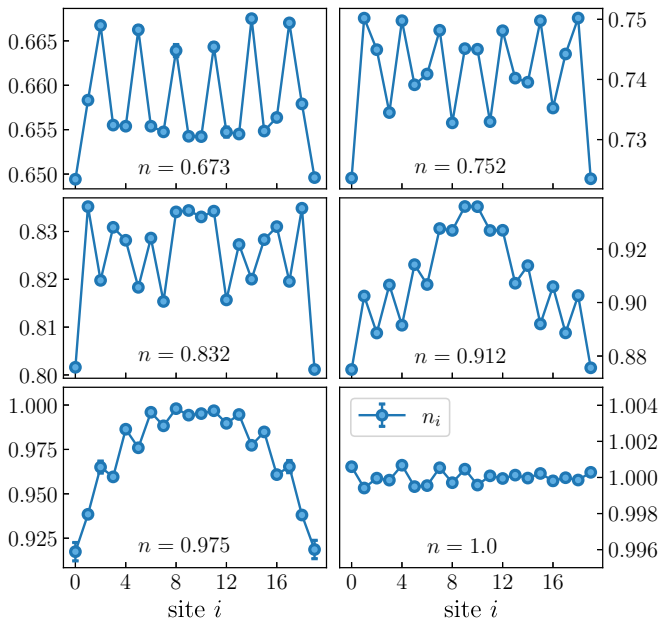


FIG. 9. Local density, n_i , versus cluster site, i , at various values of total average density for a $20 + 4$ system. A similar oscillation to the $16 + 8$ system is evident at $n = 0.673$, though with a different period, suggesting that it is indeed a finite-size effect. The local density again becomes more uniform as the average density approaches 1.0.

technique, and suggest potential improvements reserved for future work.

One of the limitations of the method is the description of the ground state. In the results presented in Fig. 3, we observe that the error in the grand potential of the cluster relative to the ED result is generally quite small, on the order of 0.1%–0.2%; however, the error bar grows in the region near the transition between the metallic and insulating states. This behavior suggests that there may be closely spaced local minima in the ground state energy landscape, which leads to a larger variance in the dVMC result. The error in the average lattice density is also largest near the transition, indicating that some of the error in the lattice Green function may come from inaccuracies, or the higher variance, of the ground state.

One means of addressing this limitation is to consider different, more flexible, variational ground state *Ansätze*, that might provide a more accurate description of the ground state [36]. The past several years have seen considerable progress in this direction, with the development of innovative variational Monte Carlo approaches, including many inspired by ideas from machine learning [37–41] or tensor networks [42,43]. The application of these approaches within dVMC remains an interesting prospect, with the potential to produce higher accuracy results for dynamical properties.

One other potential source of error in the technique is the choice of excitations, i.e., the choice of the nonorthogonal basis used to express the one particle excited sectors of the Hamiltonian. As illustrated in Fig. 3, the overall error in the average lattice density seems to depend somewhat on the accuracy of the ground state, but the ground state generally agrees quite well with the ED result. While it is difficult to disentangle the sources of error, given that the CDMFT-dVMC technique involves a self-consistency procedure comprising multiple variational minimizations, it may be possible to reduce the overall error by further optimizing the choice of excitations, as discussed in Appendix B.

V. CONCLUSION

The dVMC technique has proved to be an accurate method to compute the Green function for models of strongly correlated electrons, with and without periodic boundary conditions and translational invariance [15,16]. These previous developments laid the foundation for the approach to be implemented as an impurity solver in various quantum cluster techniques. Here we have focused on CDMFT, which includes the additional components of coupling to bath sites and the self-consistent optimization of the bath parameters.

We have introduced an impurity solver for CDMFT based on the dVMC technique and performed a systematic set of benchmarks on the single-band 1D Hubbard model. We compare against CDMFT-ED results on smaller clusters and against the Lieb-Wu solution for larger clusters. As we have shown, the approach is capable of achieving impressive accuracy (generally within 1.5% error), and, importantly, scales reasonably with system size, which makes it possible to treat large systems.

Though we have focused here on the single-band 1D Hubbard model, the approach can be applied to a wide

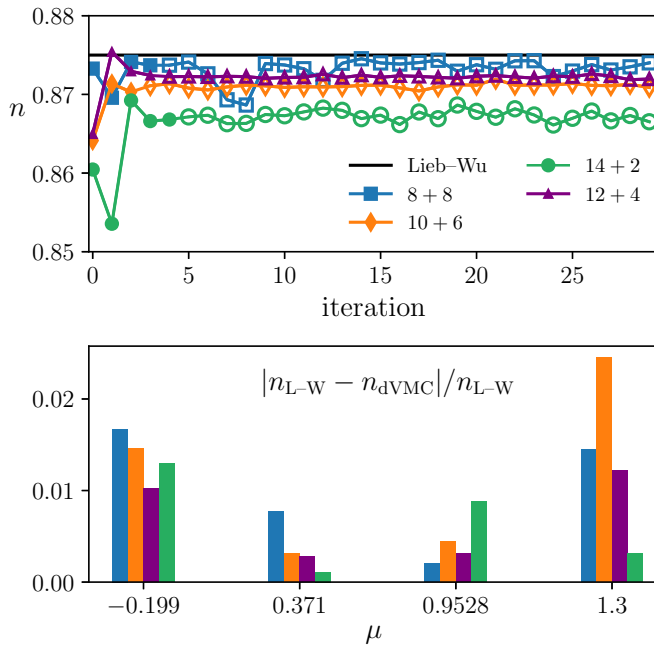


FIG. 10. Top: CDMFT-dVMC measurements of the average density versus iteration at chemical potential $\mu = 0.9528$. The open symbols indicate iterations that are included in the computation of the converged value of the average density. Bottom: Relative error with respect to the Lieb-Wu result at several values of chemical potential.

range of strongly correlated Hamiltonians, including two- and three-dimensional systems. Another goal of future work will be to extend the technique to treat superconducting systems, which requires measurement of the Nambu Green function. The ability to treat larger clusters is an important means of improving the approximation underlying quantum cluster methods. The approach we have introduced here extends the range of these already powerful methods, and holds the promise of new insights into the physics of strongly correlated electrons.

ACKNOWLEDGMENTS

P.R. was supported by a postdoctoral fellowship from the Canada First Research Excellence Fund through Institut

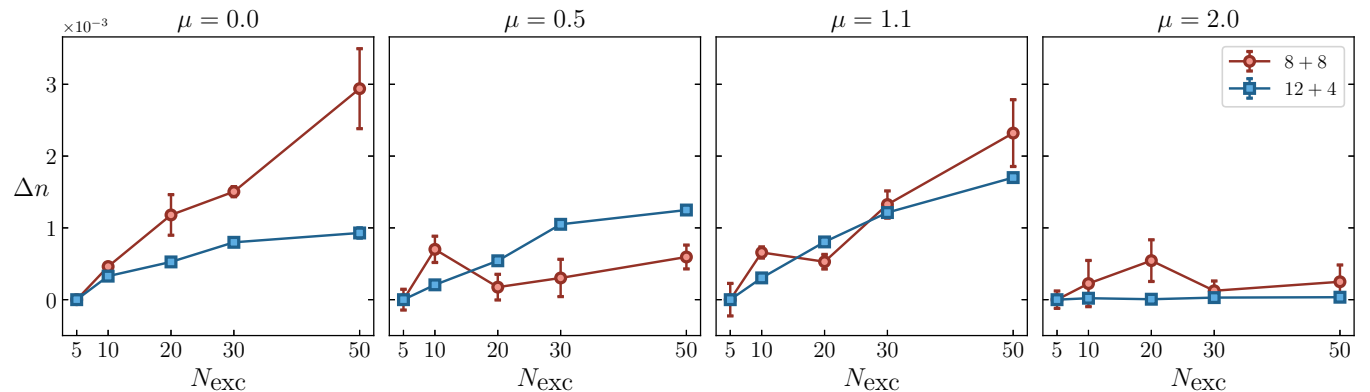


FIG. 11. Convergence versus N_{exc} . Each panel plots $\Delta n \equiv |n(N_{\text{exc}}) - n(5)|$, which gives the change in the average lattice density as a function the number of excitations, relative to the value at $N_{\text{exc}} = 5$. Note, we refer to the number of excitations included before filtering.

quantique. Computing resources were provided by the Digital Research Alliance of Canada (formerly Compute Canada) and Calcul Québec.

APPENDIX A: CONVERGENCE VERSUS NUMBER OF BATH SITES

In Fig. 10 we show several calculations of the average density for a system with a total of 16 sites, but different numbers of bath sites (See also Ref. [28]). In the upper panel we show the average lattice density computed at each iteration of the CDMFT self-consistency loop for each system. As alluded to in the main text, in the CDMFT-dVMC approach we determine convergence by inspection of the bath parameters. Once the calculation has converged we perform an additional set of iterations. The average value of an observable and the associated error bar are obtained by computing the average and standard deviation of the measurements of that observable over this set of converged iterations.

In the upper panel of Fig. 10 the converged iterations are indicated by the open symbols. For the chemical potential shown in this panel, we observe that the result for the system with the largest number of bath sites is closest to the exact result. However, this behavior is not consistent across all the values of chemical potential we have studied, as illustrated in the lower panel. For instance, while the 8+8 system is the most accurate at $\mu = 0.9528$, it is the least accurate at $\mu = -0.199$.

APPENDIX B: CONVERGENCE VERSUS NUMBER OF EXCITATIONS

In this Appendix we study the behavior of the technique as a function of the number of excitations. In Fig. 11 we show several calculations of the average lattice density for a 12+4 and an 8+8 system across a range of N_{exc} , for several values of chemical potential.

We observe that the result for the average lattice density shows relatively little dependence on the number of excitations included before filtering, as the difference between the result with $N_{\text{exc}} = 5$ and $N_{\text{exc}} = 50$ is below $\sim 5 \times 10^{-3}$, or 0.5% of the final result for the average lattice density, at all values of chemical potential studied. We observe that

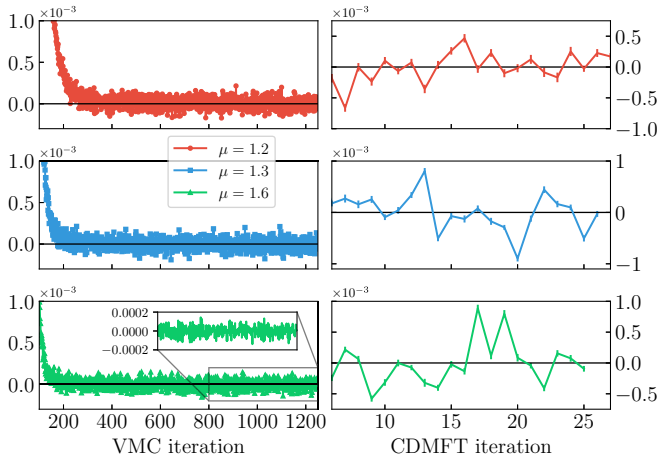


FIG. 12. Energy versus iteration for an $8 + 4$ system. The left-hand column shows the energy estimate relative to the converged value from VMC versus Monte Carlo iteration, for a single CDMFT iteration. The right-hand column shows the VMC energy estimate relative to the converged CDMFT value versus CDMFT iteration. The VMC energy standard deviation is indicated by the vertical bars. In the left-hand column, the subtracted converged values were $E_{\text{avg}} = -15.211, -16.300, \text{ and } -20.332$ for $\mu = 1.2, 1.3, \text{ and } 1.6$ respectively. And in the right-hand column, $E_{\text{avg}} = -15.208, -16.301, \text{ and } -20.333$ for $\mu = 1.2, 1.3, \text{ and } 1.6$ respectively.

the dependence is particularly small for systems within the insulating state (rightmost panel). This is true for both the $12 + 4$ and the $8 + 8$ system; however, the $8 + 8$ system has larger error bars, likely due in part to the larger number of variational parameters.

APPENDIX C: SIMULATION PARAMETERS

In this Appendix we provide typical values of the simulation parameters used to produce the results presented in the main text.

Each VMC calculation uses 1500 iterations to optimize the variational parameters of the ground state (f_{ij} , g_i , and v_{ij} of Ref. [16]). At each VMC iteration, a set of 100 thermalization samples is generated via Monte Carlo, followed by around 100 000 measurement samples of the ground state energy. Between each set of samples, the electron configurations are updated N_s times via hopping and exchange processes. After computing the ground state, we measure the Green function with dVMC using similar parameters, but perform roughly 3 000 000 Monte Carlo measurements of the matrix elements of \mathbf{S} and \mathbf{H} . Within the CDMFT loop we perform the integration over Mastubara frequencies using a sharp cutoff at $\omega_c = 2.0$ and a fictitious inverse temperature $\beta = 25$.

In order to estimate the accuracy of the results with respect to the choice of simulation parameters, we study the standard deviation of the ground state energy. In Fig. 12 we show the

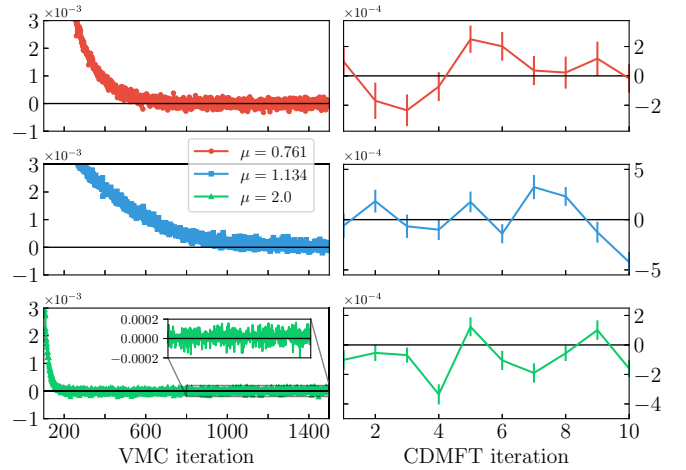


FIG. 13. Same as Fig. 12 for a $20 + 4$ system. In the left-hand column, the subtracted converged values were $E_{\text{avg}} = -28.657, -35.273, \text{ and } -56.459$ for $\mu = 0.761, 1.134, \text{ and } 2.0$ respectively. And in the right-hand column, $E_{\text{avg}} = -28.658, -35.288, \text{ and } -56.456$ for $\mu = 0.761, 1.134, \text{ and } 2.0$ respectively.

energy versus parameter optimization iteration for a system with $N_c = 8$ and $N_b = 4$. The left-hand column shows the energy estimate versus Monte Carlo iteration from the VMC calculation corresponding to the final CDMFT iteration. We plot the relative difference of the energy estimate from the converged value, $(E_{\text{avg}} - E_i)/E_{\text{avg}}$, where the converged value E_{avg} is obtained by averaging the last 50 VMC iterations and i refers to the VMC iteration. The right-hand column shows the same quantity versus CDMFT iteration, i.e., in this case E_{avg} is the average over converged CDMFT iterations, and i refers to the CDMFT iteration. The vertical bars show the standard deviation of the energy from VMC relative to E_{avg} .

We observe that the energy estimate from the VMC calculation is well converged with a standard deviation of roughly 0.2×10^{-3} in all cases shown. The fluctuations of the VMC energy versus CDMFT iteration are generally on the order of 10^{-2} , or $\sim 0.05\%$ of the average value, and larger than the standard deviation of the VMC energy at a given iteration.

To see the effect of increasing system size, we plot in Fig. 13 the same quantities as above, but for a system with $N_c = 20$ and $N_b = 4$. In this case, we find that the VMC energy converges more slowly as the system approaches the metal-insulator transition near $\mu \approx 1.4$, and the standard deviation is somewhat larger, though still on the order of 10^{-3} . This is to be expected as there is correlated metal physics found close to the Mott insulating phase, which makes for a complicated ground state energy landscape. The fluctuations of the VMC energy estimate versus CDMFT iteration are again on the order of 10^{-2} ($\sim 0.05\%$ of the average value) for all μ , but we see that the CDMFT iterations are more correlated to one another than for the smaller system.

[1] T. Schäfer, N. Wentzell, F. Simkovic, Y. Y. He, C. Hille, M. Klett, C. J. Eckhardt, B. Arzhang, V. Harkov, F. M. LeRegent, A. Kirsch, Y. Wang, A. J. Kim, E. Kozik, E. A. Stepanov,

A. Kauch, S. Andergassen, P. Hansmann, D. Rohe, Y. M. Vilks, J. P. F. LeBlanc, S. Zhang, A. M. S. Tremblay, M. Ferrero, O. Parcollet, and A. Georges, Tracking the footprints

- of spin fluctuations: A multimethod, multimessenger study of the two-dimensional Hubbard model, *Phys. Rev. X* **11**, 011058 (2021).
- [2] C. Gros and R. Valentí, Cluster expansion for the self-energy: A simple many-body method for interpreting the photoemission spectra of correlated Fermi systems, *Phys. Rev. B* **48**, 418 (1993).
- [3] D. Sénéchal, D. Perez, and M. Pioro-Ladrière, Spectral weight of the Hubbard model through cluster perturbation theory, *Phys. Rev. Lett.* **84**, 522 (2000).
- [4] D. Sénéchal, D. Perez, and D. Plouffe, Cluster perturbation theory for Hubbard models, *Phys. Rev. B* **66**, 075129 (2002).
- [5] M. H. Hettler, A. N. Tahvildar-Zadeh, M. Jarrell, T. Pruschke, and H. R. Krishnamurthy, Nonlocal dynamical correlations of strongly interacting electron systems, *Phys. Rev. B* **58**, R7475 (1998).
- [6] M. H. Hettler, M. Mukherjee, M. Jarrell, and H. R. Krishnamurthy, Dynamical cluster approximation: Nonlocal dynamics of correlated electron systems, *Phys. Rev. B* **61**, 12739 (2000).
- [7] K. Aryanpour, M. H. Hettler, and M. Jarrell, Analysis of the dynamical cluster approximation for the Hubbard model, *Phys. Rev. B* **65**, 153102 (2002).
- [8] T. A. Maier, M. Jarrell, T. Pruschke, and M. Hettler, Quantum cluster theories, *Rev. Mod. Phys.* **77**, 1027 (2005).
- [9] A. M. S. Tremblay, B. Kyung, and D. Sénéchal, Pseudogap and high-temperature superconductivity from weak to strong coupling. Towards a quantitative theory, *Low Temp. Phys.* **32**, 424 (2006).
- [10] A. I. Lichtenstein and M. I. Katsnelson, Antiferromagnetism and d -wave superconductivity in cuprates: A cluster dynamical mean-field theory, *Phys. Rev. B* **62**, R9283 (2000).
- [11] G. Kotliar, S. Y. Savrasov, G. Pálsson, and G. Biroli, Cellular dynamical mean field approach to strongly correlated systems, *Phys. Rev. Lett.* **87**, 186401 (2001).
- [12] E. Gull, A. J. Millis, A. I. Lichtenstein, A. N. Rubtsov, M. Troyer, and P. Werner, Continuous-time Monte Carlo methods for quantum impurity models, *Rev. Mod. Phys.* **83**, 349 (2011).
- [13] K. Haule, Quantum Monte Carlo impurity solver for cluster dynamical mean-field theory and electronic structure calculations with adjustable cluster base, *Phys. Rev. B* **75**, 155113 (2007).
- [14] D. Sénéchal, Bath optimization in the cellular dynamical mean-field theory, *Phys. Rev. B* **81**, 235125 (2010).
- [15] M. Charlebois and M. Imada, Single-particle spectral function formulated and calculated by variational Monte Carlo method with application to d -wave superconducting state, *Phys. Rev. X* **10**, 041023 (2020).
- [16] P. Rosenberg, D. Sénéchal, A.-M. S. Tremblay, and M. Charlebois, Fermi arcs from dynamical variational Monte Carlo, *Phys. Rev. B* **106**, 245132 (2022).
- [17] E. H. Lieb and F. Y. Wu, Absence of Mott transition in an exact solution of the short-range, one-band model in one dimension, *Phys. Rev. Lett.* **20**, 1445 (1968).
- [18] F. Tan and Q.-H. Wang, Two-mode variational Monte Carlo study of quasiparticle excitations in cuprate superconductors, *Phys. Rev. Lett.* **100**, 117004 (2008).
- [19] F. Ferrari, A. Parola, S. Sorella, and F. Becca, Dynamical structure factor of the J_1 - J_2 Heisenberg model in one dimension: The variational Monte Carlo approach, *Phys. Rev. B* **97**, 235103 (2018).
- [20] F. Ferrari and F. Becca, Spectral signatures of fractionalization in the frustrated Heisenberg model on the square lattice, *Phys. Rev. B* **98**, 100405(R) (2018).
- [21] F. Ferrari and F. Becca, Dynamical structure factor of the J_1 - J_2 Heisenberg model on the triangular lattice: Magnons, spinons, and gauge fields, *Phys. Rev. X* **9**, 031026 (2019).
- [22] K. Ido, M. Imada, and T. Misawa, Charge dynamics of correlated electrons: Variational description with inclusion of composite fermions, *Phys. Rev. B* **101**, 075124 (2020).
- [23] T. Li and F. Yang, Variational study of the neutron resonance mode in the cuprate superconductors, *Phys. Rev. B* **81**, 214509 (2010).
- [24] See Supplemental Material at <http://link.aps.org/supplemental/10.1103/PhysRevB.108.245122> for a copy of the source code developed for this study, used to produce the results in this article. This open-source code is called “dVMC-IS” and is an extension of the original “dVMC” code (Ref. [15]). Instructions are provided to compile the code and reproduce the results in Fig. 2.
- [25] T. Misawa, S. Morita, K. Yoshimi, M. Kawamura, Y. Motoyama, K. Ido, T. Ohgoe, M. Imada, and T. Kato, mVMC—Open-source software for many-variable variational Monte Carlo method, *Comput. Phys. Commun.* **235**, 447 (2019).
- [26] D. Tahara and M. Imada, Variational Monte Carlo method combined with quantum-number projection and multi-variable optimization, *J. Phys. Soc. Jpn.* **77**, 114701 (2008).
- [27] M. Caffarel and W. Krauth, Exact diagonalization approach to correlated fermions in infinite dimensions: Mott transition and superconductivity, *Phys. Rev. Lett.* **72**, 1545 (1994).
- [28] E. Koch, G. Sangiovanni, and O. Gunnarsson, Sum rules and bath parametrization for quantum cluster theories, *Phys. Rev. B* **78**, 115102 (2008).
- [29] C. J. Bolech, S. S. Kancharla, and G. Kotliar, Cellular dynamical mean-field theory for the one-dimensional extended Hubbard model, *Phys. Rev. B* **67**, 075110 (2003).
- [30] M. Capone, M. Civelli, S. S. Kancharla, C. Castellani, and G. Kotliar, Cluster-dynamical mean-field theory of the density-driven Mott transition in the one-dimensional Hubbard model, *Phys. Rev. B* **69**, 195105 (2004).
- [31] B. Kyung, G. Kotliar, and A.-M. S. Tremblay, Quantum Monte Carlo study of strongly correlated electrons: Cellular dynamical mean-field theory, *Phys. Rev. B* **73**, 205106 (2006).
- [32] M. Balzer, W. Hanke, and M. Potthoff, Mott transition in one dimension: Benchmarking dynamical cluster approaches, *Phys. Rev. B* **77**, 045133 (2008).
- [33] M. Kohno, Spectral properties near the Mott transition in the one-dimensional Hubbard model, *Phys. Rev. Lett.* **105**, 106402 (2010).
- [34] A. Liebsch and N.-H. Tong, Finite-temperature exact diagonalization cluster dynamical mean-field study of the two-dimensional Hubbard model: Pseudogap, non-Fermi-liquid behavior, and particle-hole asymmetry, *Phys. Rev. B* **80**, 165126 (2009).
- [35] A. Foley, S. Verret, A.-M. S. Tremblay, and D. Sénéchal, Coexistence of superconductivity and antiferromagnetism in the Hubbard model for cuprates, *Phys. Rev. B* **99**, 184510 (2019).
- [36] D. Wu, R. Rossi, F. Vicentini, N. Astrakhantsev, F. Becca, X. Cao, J. Carrasquilla, F. Ferrari, A. Georges, M. Hibat-Allah, M.

- Imada, A. M. Läuchli, G. Mazzola, A. Mezzacapo, A. Millis, J. R. Moreno, T. Neupert, Y. Nomura, J. Nys, O. Parcollet *et al.*, Variational benchmarks for quantum many-body problems, [arXiv:2302.04919](https://arxiv.org/abs/2302.04919).
- [37] Y. Nomura, A. S. Darmawan, Y. Yamaji, and M. Imada, Restricted Boltzmann machine learning for solving strongly correlated quantum systems, *Phys. Rev. B* **96**, 205152 (2017).
- [38] J. Han, L. Zhang, and W. E, Solving many-electron Schrödinger equation using deep neural networks, *J. Comput. Phys.* **399**, 108929 (2019).
- [39] K. Choo, A. Mezzacapo, and G. Carleo, Fermionic neural-network states for *ab-initio* electronic structure, *Nat. Commun.* **11**, 2368 (2020).
- [40] D. Pfau, J. S. Spencer, A. G. D. G. Matthews, and W. M. C. Foulkes, *Ab initio* solution of the many-electron Schrödinger equation with deep neural networks, *Phys. Rev. Res.* **2**, 033429 (2020).
- [41] J. Stokes, J. R. Moreno, E. A. Pnevmatikakis, and G. Carleo, Phases of two-dimensional spinless lattice fermions with first-quantized deep neural-network quantum states, *Phys. Rev. B* **102**, 205122 (2020).
- [42] H.-H. Zhao, K. Ido, S. Morita, and M. Imada, Variational Monte Carlo method for fermionic models combined with tensor networks and applications to the hole-doped two-dimensional Hubbard model, *Phys. Rev. B* **96**, 085103 (2017).
- [43] B. Kloss, J. Thoenniss, M. Sonner, A. Leroise, M. T. Fishman, E. M. Stoudenmire, O. Parcollet, A. Georges, and D. A. Abanin, Equilibrium quantum impurity problems via matrix product state encoding of the retarded action, *Phys. Rev. B* **108**, 205110 (2023).